v. 5, n. 2, 2025

Journal of Engineering Research

Acceptance date: 21/02/2025

BOOSTING THE CATALYTIC EFFICIENCY OF VANADIUM-DOPED TITANIUM DIOXIDE NANOPARTICLES FOR ENVIRONMENTAL APPLICATIONS

Benedito Donizeti Botan-Neto
Laboratório de Plasmas e Processos (LPP), Instituto Tecnológico de Aeronáutica (ITA), São José dos Campos, SP, Brazil
Departamento de Física Aplicada-ICMUV, MALTA Consolider Team, Universitat de València, Burjassot, Spain

Helen Caroline de Souza Barros
Laboratório de Plasmas e Processos (LPP), Instituto Tecnológico de Aeronáutica (ITA), São José dos Campos, SP, Brazil

Armstrong Godoy-Junior
Laboratório de Plasmas e Processos (LPP), Instituto Tecnológico de Aeronáutica (ITA), São José dos Campos, SP, Brazil

Marcilene Cristina Gomes
Instituto Federal de Educação, Ciência e Tecnologia de São Paulo (IFSP), São José dos Campos, SP, Brazil

Argemiro Soares da Silva Sobrinho
Laboratório de Plasmas e Processos (LPP), Instituto Tecnológico de Aeronáutica (ITA), São José dos Campos, SP, Brazil

Douglas Marcel Gonçalves Leite
Laboratório de Plasmas e Processos (LPP), Instituto Tecnológico de Aeronáutica (ITA), São José dos Campos, SP, Brazil

Gilberto Petraconi Filho
Laboratório de Plasmas e Processos (LPP), Instituto Tecnológico de Aeronáutica (ITA), São José dos Campos, SP, Brazil

Rodrigo Sávio Pessoa
Laboratório de Plasmas e Processos (LPP), Instituto Tecnológico de Aeronáutica (ITA), São José dos Campos, SP, Brazil

André Luis de Jesus Pereira
Laboratório de Plasmas e Processos (LPP), Instituto Tecnológico de Aeronáutica (ITA), São José dos Campos, SP, Brazil

Abstract: The contamination of water resources by industrial pollutants, particularly organic dyes, poses a severe threat to ecosystems and public health. Addressing this challenge requires the development of efficient and sustainable technologies for wastewater treatment. Among these, the use of advanced catalytic materials has gained significant attention due to their potential to degrade complex pollutants under mild conditions. In this study, we investigate pure and vanadium-doped TiO_2 nanoparticles, synthesized via the modified Pechini method with varying vanadium percentages for methylene blue (MB) dye adsorption-based degradation. Detailed structural and chemical analyses revealed that vanadium doping enhances the material's surface area, modifies its electronic properties, and increases the concentration of oxygen vacancies, all of which contribute to improved catalytic performance. The 3.1 mol% vanadium-doped TiO_2 sample demonstrated a remarkable 679.5% improvement in degradation efficiency compared to its undoped counterpart. Kinetic and thermodynamic studies further elucidated the mechanisms driving this enhancement. These results underscore the potential of vanadium-doped TiO_2 as a high-performance, environmentally friendly solution for wastewater remediation.
Keywords: Water contamination, vanadium-doped TiO_2, sustainable catalysis, wastewater treatment, adsorption kinetics.

INTRODUCTION

Industries such as textiles, paper, plastics, food, pharmaceuticals, and cosmetics are major sources of dye-contaminated wastewater, which poses significant environmental challenges [1–4]. Dye pollution in aquatic environments reduces water clarity, depletes dissolved oxygen, hinders aquatic life development, and poses health risks, including cancer [5–7]. Among these pollutants, Me-

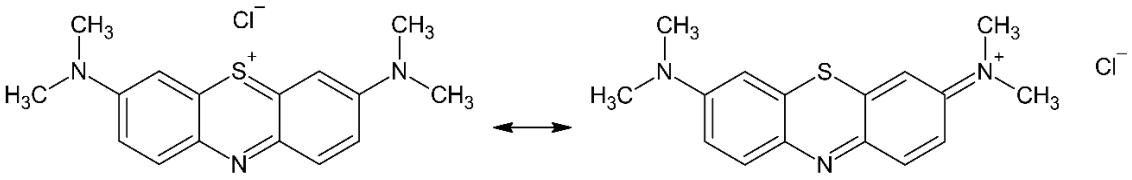

Figure 1. Structure of Methylene Blue (MB). **(Left)** Sulfur (S) as a cation due to the proximity of Chlorine (Cl). **(Right)** Nitrogen (N) as a cation due to the proximity of Cl with the amine group.

thylene Blue (MB) is a heterocyclic cationic azo dye that is particularly difficult to remove from wastewater due to its complex aromatic structure, which contains chromophores and a polar group in the central ring [3,4,8]. **Figure 1** illustrates two possible structures of MB, resulting from π-delocalization.

New approaches to addressing water contamination are being explored, with the Advanced Oxidation Process (AOP) emerging as a viable option. AOP involves water purification through oxidation, often attributed to hydroxyl radicals (OH•) that attack organic compounds via radical addition, hydrogen abstraction, electron transfer, and/or radical combination [4,9,10]. AOP encompasses various techniques, including homogeneous and heterogeneous catalysis/photocatalysis, Fenton and Fenton-like processes, ozonation, and electrochemical methods [9,11].

Heterogeneous AOP processes, such as adsorption, have gained attention due to their high efficiency in organic dye degradation, simplicity, reproducibility, and cost-effectiveness. An effective catalyst for adsorption must exhibit key properties such as a large specific surface area, porous structure, chemical and physical stability, and non-toxicity [5,9–11]. Titanium dioxide (TiO_2) is a well-studied material for such applications, owing to its non--toxicity, chemical and thermal stability, and low cost [12–15]. While TiO_2 demonstrates good catalytic and photocatalytic degradation activity, its performance can be enhanced through doping, which involves incorporating small amounts of metallic oxides or cations into the material's structure [16,17]. Among transition metals, vanadium (V) is particularly suitable for doping TiO_2 due to its similar atomic radius to titanium, facilitating substitutional incorporation into the TiO_2 lattice when in the same valence state [16,18–23].

TiO_2 can be synthesized using various methods, including solid-state reaction, chemical vapor deposition (CVD), electrodeposition, sonochemical techniques, sol-gel, Pechini method, hydrothermal, and solvothermal approaches [1,24–26]. The Pechini method, also known as the Polymeric Precursor Method, is widely used for producing metal oxide nanoparticles due to its simplicity, high efficiency, low cost, and ability to generate high-purity, homogeneous nanoparticles [27–29]. This method involves polyesterification of a metal cation, typically chelated with citric acid and polymerized with a glycol group [27,30–32].

Despite extensive research on TiO_2 photocatalysis, relatively little is known about the adsorption process of MB on the surface of V-doped TiO_2 nanoparticles. Understanding this adsorption mechanism is crucial as it directly influences the efficiency of the overall photocatalytic process. Adsorption is a temperature-dependent, reversible process, either physical (physisorption) or chemical (chemisorption), where a guest molecule (adsorbate) attaches to the adsorbent's surface. Physisorption typically occurs due to weak attraction forces, while chemisorption involves the formation of chemical bonds.

This study aims to synthesize and characterize pure and vanadium-doped TiO_2 nanoparticles with varying vanadium doping percentages, using the modified Pechini method,

to evaluate their effectiveness in MB degradation via adsorption. This work contributes to a deeper understanding of MB adsorption on V-doped TiO_2 surfaces, complementing investigations into its photocatalytic properties. Various characterization techniques were employed to assess chemical, morphological, structural, and vibrational properties. Additionally, adsorption tests were conducted in 10 $mg.L^{-1}$ MB solutions to evaluate and optimize the catalytic activity of the samples.

MATERIAL AND METHODS

SYNTHESIS OF $Ti_{1-x}(V)_xO_2$ NANOPARTICLES

Titanium citrate was synthesized using the modified Pechini method. Titanium (IV) isopropoxide (TTIP) ($Ti[OCH(CH_3)_2]_4$) (Alfa Aesar, 97%) was mixed with citric acid monohydrate (CA) ($C_6H_8O_7.H_2O$) (Synth, 99.5%), previously dissolved in deionized water, at a CA:TTIP molar ratio of 2:1. The mixture was kept at 70 °C under vigorous stirring. Vanadium doping was introduced by adding ammonium metavanadate (NH_4VO_3) (Anidrol, 98%) at various concentrations (0.2%, 0.5%, 1%, 2%, 3%, and 5%) into the titanium citrate solution. The polymerization of the titanium citrate to form a resin was achieved by adding ethylene glycol (EG) ($C_2H_6O_2$) (Proquimios, 99.5%) in a weight ratio of 40:60 (EG), while maintaining the system at 100 °C with continuous stirring. The resulting greenish resin was then subjected to pyrolysis at 300 °C for 2 hours (with a heating ramp of 10 $°C.min^{-1}$) and subsequently calcined at 500 °C for 2 hours (also with a 10 $°C.min^{-1}$ heating ramp) to produce $Ti_{1-x}V_xO_2$ nanoparticles.

CHARACTERIZATION AND MEASUREMENTS

The morphology of the synthesized nanoparticles was examined using scanning electron microscopy (SEM-FEG) on a Mira 3 Tescan microscope, operating at a beam intensity of 10 keV with a magnification of 200 kx, and utilizing secondary electron mode. To further investigate the chemical composition, energy-dispersive X-ray spectroscopy (EDX) was performed using an Oxford Instruments system coupled to a Vega 3 Tescan microscope. The phase composition and microstructural characteristics of the nanoparticles were analyzed using powder X-ray diffraction (XRD) and Raman spectroscopy. XRD measurements were conducted on an Empyrean PANalytical diffractometer equipped with a copper X-ray source and a Cu Kα monochromator (λ = 0.1542 nm), operating in Theta-2Theta mode with the sample stage rotating at 16 rpm. Raman spectroscopy was carried out using a Horiba Evolution spectrometer with a 532 nm laser, a grating of 600 $lines.mm^{-1}$, and an acquisition time of 30 seconds with 2 accumulations. X-ray photoelectron spectroscopy (XPS) was performed using a Thermo Scientific K-Alpha spectrometer, operating at 120 W with an Al Kα excitation source (hν = 1486.69 eV), to investigate the binding energies and chemical composition of the material.

ADSORPTION TEST

The adsorption test was conducted using methylene blue dye (MB - $C_{16}H_{18}ClN_3S{\cdot}xH_2O$) (Neon C.I. 52015) without prior purification. A 10 $mg.L^{-1}$ MB solution (pH = 5) was prepared using deionized water and stored in a flat-bottom flask covered with black electrical tape to prevent light exposure. The test involved adding 32 mg of the catalyst to 64 ml of the MB solution, and the mixture was left in the dark for 2.5 hours to reach adsorption equilibrium. At specific time intervals, 2

ml aliquots were withdrawn and immediately analyzed using a UV-Visible spectrophotometer (Evolution 220) in the wavelength range of 190-1100 nm. The degree of MB degradation was determined by monitoring the absorbance at 665 nm.

RESULTS AND DISCUSSION

CHEMICAL AND MORPHOLOGICAL PROPERTIES

Chemical composition tests using EDX were conducted to assess the relationship between the calculated molar vanadium doping percentage ($V_{theoretical}$) and the actual incorporated vanadium molar percentage ($V_{incorporated}$). **Table 1** summarizes these values, and sample IDs were assigned for clarity in discussing and presenting the data. The incorporation rate of vanadium ($dV_{incorporated}/dV_{theoretical}$) was found to be approximately 0.6(1)% (**Figure S1**).

Sample ID	$V_{theoretical}$ (%)	$V_{incorporated}$ (%)	Bandgap (eV)
Undoped TiO_2	0.0	0	3.16
0.5% V	0.2	0.5(1)	2.44
0.6% V	0.5	0.6(1)	2.20
0.7% V	1.0	0.7(1)	2.39
1.3% V	2.0	1.3(2)	2.47
2.0% V	3.0	2.0(2)	2.53
3.1% V	5.0	3.1(2)	-

Table 1. Relationship between the calculated and incorporated vanadium doping percentage and the corresponding bandgap for each sample.

XPS measurements were performed to analyze the oxidation states of Ti 2p, O 1s, and V 2p (survey spectra are shown in **Figure S2**). **Figure 2a** shows the high-resolution XPS spectra of Ti 2p, with peaks at approximately 465 eV and 459 eV, corresponding to the Ti $2p_{1/2}$ and Ti $2p_{3/2}$ levels in the oxidation state Ti^{+4} [33,34] regardless of the vanadium doping percentage. **Figure 2b** depicts the asymmetric O 1s spectra requiring two Gaussian curves to fit the profile. The curve centered at approximately 530.6 eV, corresponds to oxygen vacancies ($V_O^{\bullet}$) signal. In principle, the $V_O^{\bullet}$ signal corresponds to the signal of hydroxyl from atmospheric water, which is spontaneously adsorbed in the metal oxide, at ambient conditions. XPS cannot measure a vacancy since it is based on the kinetic energy of an electron withdrawn from an atom's core or valence states [35–37]. The *inset* in the Figure 2b, depicts the $V_O^{\bullet}$ concentration, as a function of vanadium doping percentage. V $2p_{3/2}$ spectra are displayed in **Figure 2c** (note that the 0.6% V sample is not there, since the weak signal obtained during the measurements, made it impossible to fit the experimental data). The peak centered at approximately 516 eV, indicates that the vanadium was incorporated in a substitutional way in the TiO_2 lattice [33]. The fitting of the XPS spectra, up to 0.7% V doping, shows only the presence of the V^{3+} (centered at 515.8 eV); after this concentration, the spectra must be fitted using two Gaussian curves, with the additional curve attributable to the V^{5+} (517 eV) [33,38]. High-resolution XPS measurements of the Valence Band of the TiO_2, allow us to estimate the bandgap by extrapolating from the low-energy linear region [39,40]. **Figure 2d** depicts the region and the extrapolation (dashed lines), with bandgap values available in Table 1. Furthermore, the *inset* in Figure 2d depicts the evolution of the bandgap as a function of vanadium doping percentage.

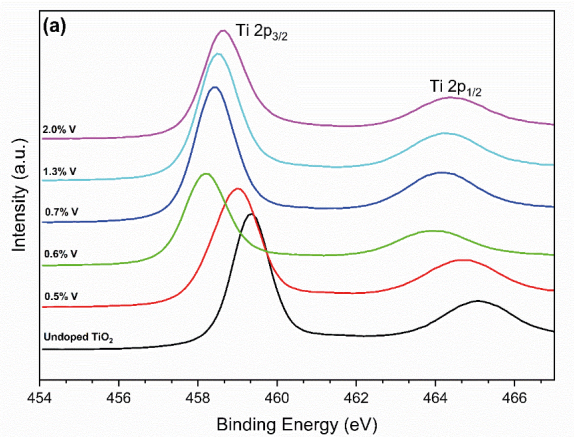

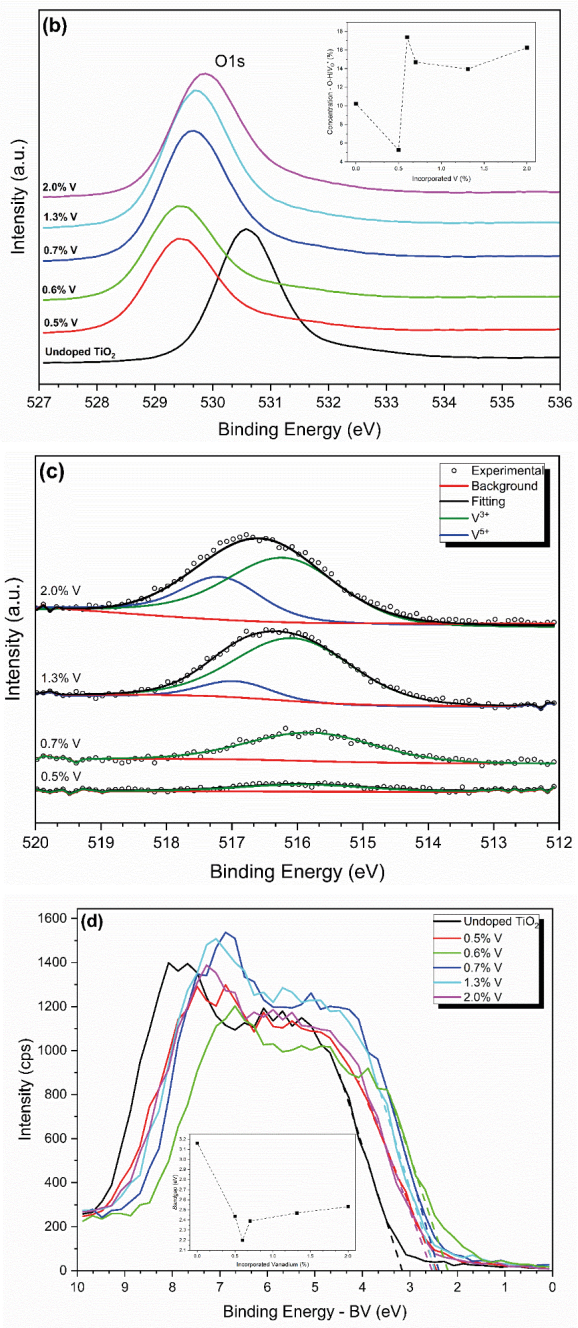

Figure 2. a) High-resolution Ti 2p spectra. **b)** High-resolution spectra O 1s spectra (inset: Oxygen vacancies ($V_O^{\bullet}$) as a function of vanadium doping). **c)** High-resolution V $2p_{3/2}$ spectra (open circles: experimental data, solid lines: fitted data). **d)** Valence Band position measured by XPS (solid line: experimental data, dashed line: extrapolation of the low-energy linear region; inset: bandgap as a function of vanadium doping). (Dashed lines were employed in the insets to facilitate interpretation of the data).

Vanadium doping does not modify the titanium oxidation state but decreases the energy binding (**Figure S3**) up to 0.7%, percentages greater than this, increasing the binding energy slightly. Vanadium can reduce binding energy in oxygen up to 0.5%, after that, it increases the binding energy slightly (**Figure S4**). The behavior observed with the binding energy is inverse to the behavior observed with the $V_O^{\bullet}$. The $V_O^{\bullet}$ increases up to 0.5%, then begins to decrease. The explanation for this occurrence is the appearance of V^{5+} in the structure because the $V_O^{\bullet}$ is generated by the doping with an element with a lower oxidation state (V^{3+}) compared with the titanium (Ti^{4+}) [41]. The anatase bandgap reported in the literature is 3.2 eV [42]. The effects observed with decreasing bandgap are related to vanadium doping, which causes the creation of unoccupied defect states and Urbach tails in the material's band structure [41–43].

Figure 3 shows SEM images arranged by vanadium doping percentage. Vanadium doping does not affect the morphology of TiO_2, allowing for the observation of spherical nanoparticle agglomerations. It is feasible to see that the agglomeration range is rather lengthy up to 2.0%, but it becomes more discontinuous at 3.1%. Regardless of the vanadium doping percentage, the average nanoparticle size is 20 nm. Traditionally, V-doped TiO_2 is synthesized via sol-gel, which results in large grains with low specific surface area and the risk of segregation and precipitation. Alternatively, the Pechini method produces tiny grains with a high specific surface area, with no segregation or precipitation [32]. The chemical analyses performed in this study are sufficient to prove and demonstrate the effectiveness of using the Pechini Method in V-doped TiO_2 synthesis.

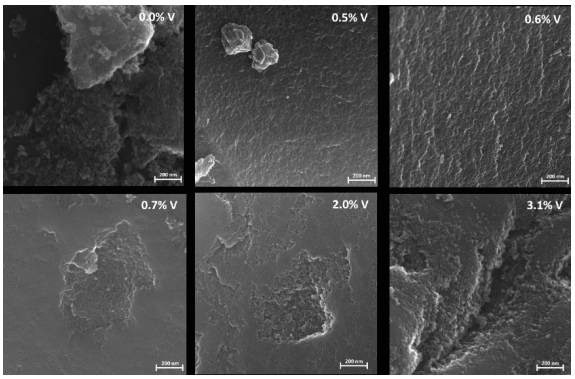

Figure 3. SEM-FEG Images of V-doped TiO_2 samples. **(a)** Undoped TiO_2, **(b)** 0.5% V, **(c)** 0.6% V, **(d)** 0.7% V, **(e)** 2.0% V, **(f)** 3.1% V.

STRUCTURAL AND VIBRATIONAL PROPERTIES

According to the literature, the most stable crystalline phase of undoped TiO_2 nanoparticles is the tetragonal ($I4_1/amd$) anatase phase, with Z = 4, and lattice parameters a = 3.7842(13) Å, c = 9.5146(15) Å, and V = 136.25 Å³ [44]. **Figure 4a** depicts XRD patterns. The patterns show that TiO_2 crystallizes in the anatase phase regardless of vanadium doping percentage, and the absence of vanadium oxide (V_2O_5) peaks indicates that vanadium was incorporated into the lattice.

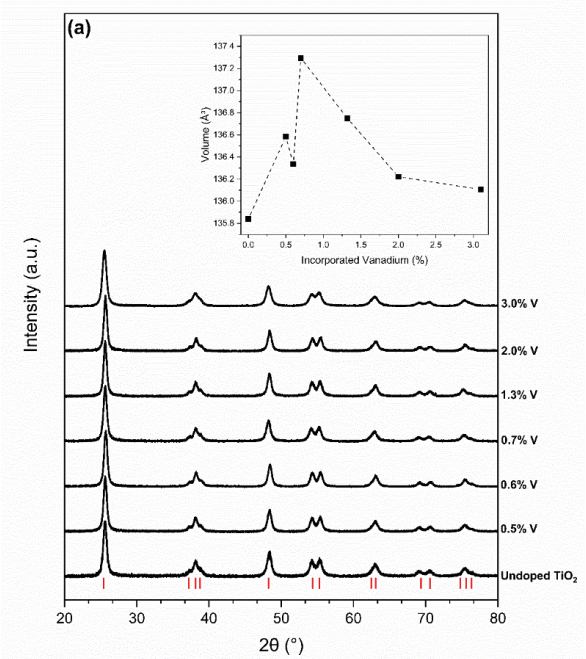

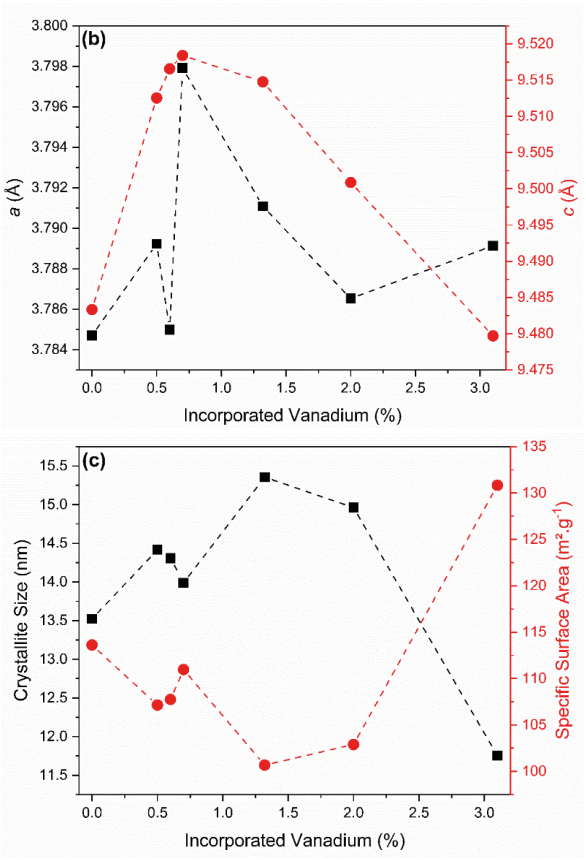

Figure 4. a) XRD patterns of V-doped samples (red ticks depict the Bragg positions of the anatase phase). (*inset*) Unit cell volume as a function of vanadium doping percentage. **b)** Lattice parameters a (black squares) and c (red circles) as a function of vanadium doping percentage. **c)** Crystallite size (black squares) and specific surface area (red circles) as a function of vanadium doping percentage. (Dashed lines were employed to facilitate interpretation of the data.)

The lattice parameters were acquired by indexing the reflections using UnitCell Software [45]. **Table 2** summarizes the lattice parameters, the crystallite size, the density, and the specific surface area. The *inset* in Figure 3a represents the unit cell volume as a function of vanadium doping percentage. XPS investigations indicate that up to 0.7% vanadium doping results in only the presence of V^{3+} (0.78 Å), which is slightly larger than Ti^{4+} (0.745 Å) [46], leading to an increase in cell volume. Above this vanadium doping percentage, the

Sample ID	Volume (Å^3)	*a* (Å)	*c* (Å)	Crystallite Size (nm)	Density (g.cm^{-3})	Specific Surface Area (m^2.g^{-1})
Undoped TiO_2	135.84(2)	3.7847(2)	9.4834(6)	13.52	3.91	114
0.5% V	136.59(2)	3.7893(2)	9.5126(6)	14.42	3.88	107
0.6% V	136.34(2)	3.7850(2)	9.5166(6)	14.31	3.89	108
0.7% V	137.30(2)	3.7980(2)	9.5185(6)	13.99	3.86	111
1.3% V	136.75(2)	3.7911(2)	9.5148(6)	15.35	3.88	101
2.0% V	136.23(2)	3.7866(2)	9.5009(6)	14.96	3.90	103
3.1% V	136.11(2)	3.7892(2)	9.4797(6)	11.75	3.90	131

Table 2. Indexed lattice parameters, crystallite size, density, and specific surface area obtained by XRD of V-doped samples.

presence of V^{5+} (0.68 Å) promotes a decrease in cell volume, following the difference in atomic radii. The same trend is shown in **Figure 4b**, which illustrates the *a* and *c* lattice parameters. The *a* axes, change with no specific tendency according to the vanadium percentage. In contrast, the *c* axes behave "linearly" with the presence of $V^{3+/5+}$, which is explained by the substitution of the Ti^{4+} by $V^{3+/5+}$, preferentially in the body-centered (*I*) lattice sites of the anatase structure [47].

Powder samples' crystallite size (D) was estimated by using the Scherrer Equation to the diffraction angle of the crystal plane (101) (2θ ~ 25.4°) [14,18,19]. The equation is as follows:

$$D = \frac{0.9\lambda}{\beta \cos\theta} \quad (1)$$

where **λ** is the X-Ray wavelength (λ = 0.1542 nm), and β is the Full Width at Half Maximum (FWHM) in degrees, of the (101) reflection. **Figure 4c** depicts the variation in crystallite size as a function of vanadium doping percentage. The behavior is like the stated volume and lattice parameters, with an increase up to 0.7% vanadium doping, followed by a drop above this concentration. At 3.1% we observe crystallite sizes smaller than in the undoped sample.

Crystallite size calculations allow for the estimate of the specific surface area (S_a) of the samples using the following equation [47]:

$$S_a = \frac{6}{D \times \rho} \quad (2)$$

where **ρ** is the sample's density. Figure 4c also depicts specific surface areas, which show behavior inversely related to crystallite size, demonstrating that increasing vanadium concentration leads to samples with reduced surface areas as compared to the undoped sample. However, the sample 3.1% doped, had a surface area 14.9% larger than the undoped sample. Choi [49], reported Brunauer-Emmett-Teller (BET) surface area measurements of TiO_2 synthesized using the Sol-Gel Method and calcined at 400 °C, presenting a surface area of 104 m^2.g^{-1}, while a sample with 0.3% vanadium doped has 132 m^2.g^{-1}. In the current study, our undoped nanoparticles are slightly larger, while doped nanoparticles with 0.5/0.6/0.7% vanadium doping are smaller.

Figure 5 depicts the anatase Raman spectra of vanadium-doped samples. Symmetry analysis of anatase reveals 27 vibrational modes at the Brillouin zone center (Γ). The mechanical decomposition of these modes includes: $\Gamma = 2A_{1g}(R) + 2B_{1g}(R) + B_{2g}(R) + 3E_g(R) + 3A_{2u}(IR) + 5E_u(IR) + 2A_{1u} + 2B_{1u} + 4B_{2u} + A_{2g} + A_{2u} + E_u$, consisting of 25 optical modes (which contains 8 active Raman (R) modes and 8 active infrared (IR) modes) and two acoustic modes [50]. In the literature, factor group analysis reveals 15 optical modes with irreducible representation $A_{1g}(R) + 2B_{1g}(R) + 3E_g(R) + A_{2u}(IR) + 2E_u(IR) + B_{2u}(IR)$, including 6 active Raman modes and 3 active infrared modes [51,52].

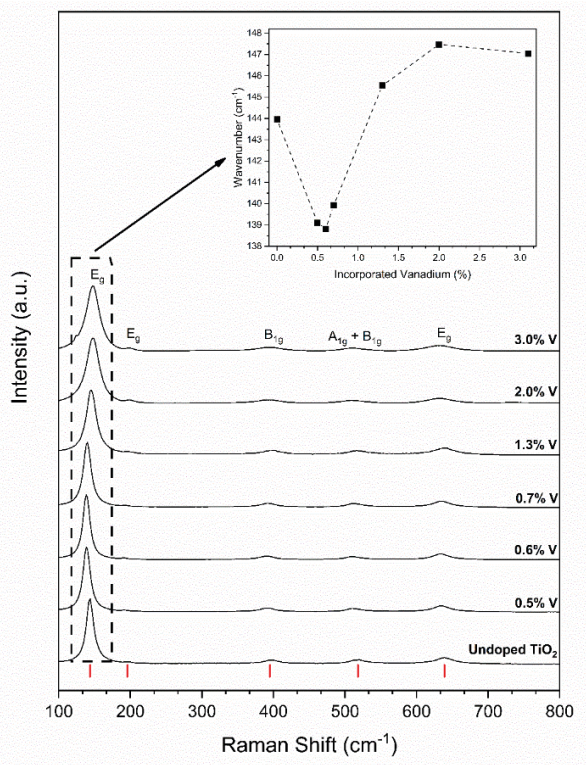

Figure 5. Raman spectra of vanadium-doped samples (red ticks depict the Raman modes of the anatase phase). (inset) E_g peak position as a function of vanadium doping percentage. (Dashed lines were employed to facilitate interpretation of the data.)

Raman results are consistent with XRD results, demonstrating the absence of vanadium oxide, and confirming the presence of only the anatase phase. According to the literature, the anatase vibrations correspond to those at 144 cm^{-1} (E_g), 196 cm^{-1} (E_g), 395 cm^{-1} (B_{1g}), 518 cm^{-1} (A_{1g} + B_{1g}), and 639 cm^{-1} (E_g) [52,53], which explains the modes found in our Raman spectra. The main vibrational mode in anatase is the mode E_g at 144 cm^{-1}, which corresponds to the symmetric stretching vibration O – Ti – O [54]. As a result, the *inset* in Figure 5 shows the evolution of the wavenumber of the E_g mode as a function of the vanadium doping percentage. A *redshift* can be observed in samples with up to 0.7% vanadium doping. According to the XRD results, the observed shift in the sample is related to the larger unit cell. *Blueshift* can be observed in samples with doping percentages above 0.7%, related to a slight decrease in the unit cell volume. All these results support the XPS results regarding vanadium's oxidation state incorporated into the TiO_2 lattice and oxygen vacancies [51,55].

ADSORPTION TEST

Adsorption is a reversible, temperature-dependent physical or chemical superficial process in which a guest molecule (adsorbate) attaches or adheres to the adsorbent's surface. Adsorption is classified as physisorption, or chemisorption based on the mechanism observed between the adsorbent and the adsorbate. In general, physisorption occurs due to attraction forces, whereas chemisorption occurs via chemical bonding [56–58].

Preliminary experiments were carried out using only MB, to assess the MB degradation owing to stirring, in the absence of a catalyst. **Figure 6a** depicts the experiment, represented by the navy-blue pentagons, and after 150 minutes, the MB degradation was 1.86%. An overview of the MB degradation reveals the hole of vanadium doping, which is responsible for the increased adsorption activity of TiO_2. The MB degradation percentages for vanadium-doped samples at 0.0, 0.5, 0.6, 0.7, 1.3, 2.0, and 3.1% are 8.3, 7.03, 11.6, 26.5, 41.7, 54.1, and 64.7%, respectively.

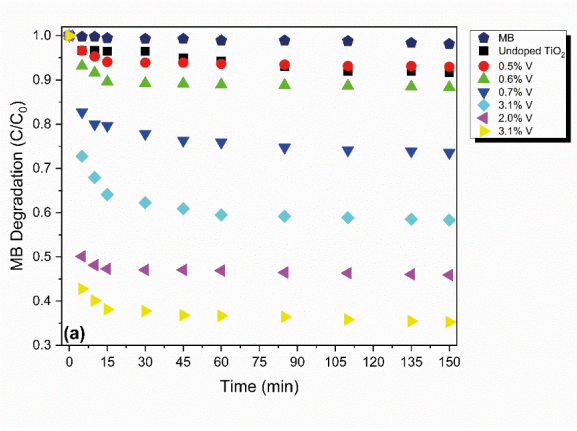

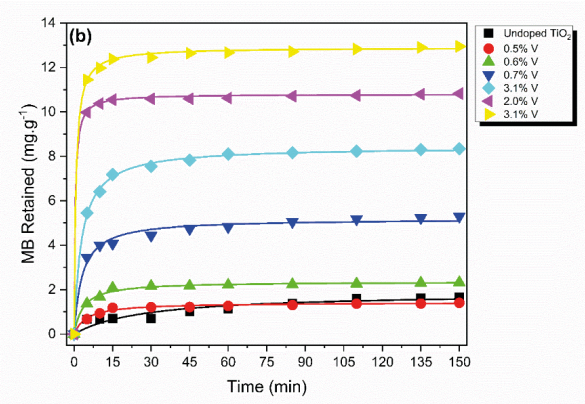

Figure 6. a) Methylene Blue (MB) degradation via adsorption in vanadium-doped samples. Navy-blue pentagons depict the self-degradation of MB through stirring. **b)** The amount of MB retained per gram of adsorbent in vanadium-doped samples. Symbols represent experimental data, while solid lines reflect the Pseudo-Second Order (PSO) fitting.

It is possible to observe that the highest adsorption of MB happens within the first five minutes, indicating a highly quick process. To assess the adsorption capacity for MB, the experimental amount of MB retained per gram of adsorbent (Q) at the instant t [59,60], was calculated as follows:

$$Q(t) = \frac{(C_0 - C_t).V}{m} \quad (3)$$

where C_0 is the initial concentration of MB, C_t is the concentration of MB at the instant t, V is the MB solution volume and m is the mass of the adsorbent. A non-linear kinetic model was used to fit and evaluate the adsorption velocity into the adsorbent, as well as the adsorbent's performance in the Pseudo-First Order (PFO) and Pseudo-Second Order (PSO) models [61]. The PFO model can be defined as:

$$Q(t) = Q_e(1 - e^{-k_1 t}) \quad (4)$$

where k_1 is the pseudo-first-order rate constant (min^{-1}) and Q_e is the amount of MB retained per gram of adsorbent at the equilibrium (110 min in the present study). While the PSO model can be described as follows:

$$Q(t) = \frac{{Q_e}^2 k_2 t}{1 + Q_e k_2 t} \quad (5)$$

where k_2 is the pseudo-second-order rate constant ($g.mg^{-1}.min^{-1}$).

Figure 6b, depicts the experimental Q(t) data by symbols, as can be seen, the results are inversely proportional to the results observed in Figure 6a, which makes sense given that MB degradation occurs due to the occupancy of active sites on the catalyst's surface. **Table 3** shows each sample's q_e, rate constants, and R^2 after fitting the experimental data with PFO and PSO models. Statistically, the PSO model (shown by solid lines in Figure 6b) better describes MB adsorption with TiO_2. The PSO model states that the adsorption rate is proportional to the amount of MB retained at equilibrium and at any given time. This model demonstrates that the rate-limiting step is the chemical interaction between the MB molecules and the TiO_2 active sites [7].

The PSO model is responsible for describing the kinetic behavior of the MB degradation, and when we look to k_2, we can see that the best catalyst kinetically, is the 2.0% vanadium doping, which contradicts the results shown in Figure 6a, which shows the 3.1% vanadium doping as the best catalyst. The reason for this mismatch is the difference between kinetic and thermodynamic stability. To assess the thermodynamic stability, the Adsorption Potential (A) [58,62], is calculated as follows:

$$A = -RT \ln \frac{C_0}{C_e} \quad (6)$$

where R is the universal gas constant (8.314 $J.mol^{-1}.K^{-1}$), T is the temperature (298.15 K), and C_e is the MB's equilibrium concentration.

The adsorption potential describes a catalyst's capability. A negative adsorption potential means that the adsorbate will move to the region with a lower adsorption potential (adsorbent), and this reaction is thermodynamically stable and favored, lowering the sys-

Sample ID	$Q_{e,exp}$ (mg.g^{-1})	Adsorption Potential (kJ.mol^{-1})	PFO Model			PSO Model		
			k_1 (min^{-1})	$Q_{e,fit}$ (mg.g^{-1})	R^2	k_2 (g.mg^{-1}.min^{-1})	$Q_{e,fit}$ (mg.g^{-1})	R^2
Undoped Ti_O2	1.60	-0.21	0.03	1.60	0.892	0.02	1.87	0.906
0.5% V	1.37	-0.18	0.13	1.32	0.980	0.14	1.42	0.987
0.6% V	2.27	-0.31	0.17	2.24	0.989	0.12	2.36	0.992
0.7% V	5.17	-0.76	0.19	4.90	0.953	0.06	5.19	0.987
1.3% V	8.23	-1.34	0.19	8.02	0.983	0.04	8.43	0.999
2.0% V	10.7	-1.93	0.54	10.6	0.999	0.24	10.8	0.999
3.1% V	12.8	-2.58	0.45	12.6	0.996	0.12	12.9	0.999

Table 3. Kinects (Q_e, k_1 and k_2) and thermodynamic (adsorption potential) parameters determined experimentally and fitted (Pseudo-First Order (PFO) and Pseudo-Second Order (PSO) models) of MB degradation using V-doped samples.

tem's Gibbs Free Energy. The adsorption capacity can be found in Table 3. The meaning of k_2 and adsorption potential explains the different kinetic and thermodynamic results. The k_2 is responsible for explaining the kinetics of reaching the system's equilibrium condition, so the highest value of k_2 to the 2.0% vanadium doping indicates that the equilibrium is reached first, as compared to the other samples, and that this sample is more stable kinetically. Furthermore, the adsorption potential suggests that 3.1% vanadium doping is the best catalyst, resulting in faster degradation of MB at constant temperature in the shortest time interval, implying that this sample is thermodynamically more stable than others.

The enhancement of TiO_2 samples through vanadium doping is explained in different ways. Chemically, vanadium doping improves catalytic activity by increasing superficial hydroxyl groups ($V_0^{\bullet}$ concentrations), electron transfer, and porosity, resulting in faster interactions between the adsorbate and the adsorbent [9,58,63]. Figure 2b and Figure 3, show the increase in superficial $OH^{\bullet}$ and porosity, respectively. The reaction for MB degradation by $OH^{\bullet}$, is as follows:

$$MB + OH^{\bullet} \rightarrow CO_2 + H_2O + intermediaries \quad \text{(R1)}$$

Structurally, vanadium doping causes changes in specific surface area due to lattice changes. Combining chemical and structural modifications of vanadium doping is the key to MB adsorption employing V-doped TiO_2. 3.1% vanadium doping had the highest degradation activity (64.7%), with a specific surface area of 131 $m^2.g^{-1}$. This represents a 14.9% increase over the undoped sample, resulting in a 679.5% increase in degradation activity. The vanadium hole is visible in the TiO_2 structure.

CONCLUSION

The current study has demonstrated significant advancements in the synthesis and application of V-doped TiO_2 nanoparticles using the modified Pechini method. This method has proven to be highly efficient, enabling the substitutional incorporation of vanadium into the TiO_2 lattice with different valence states (V^{3+}/V^{5+}) and a predicted incorporation rate of 0.6% per mol. Vanadium incorporation resulted in structural and vibrational changes, particularly affecting the specific surface area and oxygen vacancy () concentrations, which are crucial for enhancing the material's adsorption properties. The study showed that vanadium doping effectively improves the catalytic performance of TiO_2, particularly in the degradation of MB through adsorption. Structural analysis confirmed that the anatase phase of TiO_2 was preserved across all doping levels, with no evidence of vanadium oxide formation. The 3.1% V-doped sample

exhibited the most significant enhancement, with a 679.5% increase in degradation activity compared to undoped TiO_2, attributed to increased surface area and optimized bandgap. Kinetic and thermodynamic studies revealed that the adsorption process follows a PSO model. While the 2.0% V-doped sample showed the highest kinetic stability, the 3.1% V-doped sample demonstrated superior thermodynamic stability and overall adsorption capacity. These findings highlight the potential of vanadium-doped TiO_2 as a promising material for environmental remediation, particularly in treating dye-contaminated wastewater.

SUPPORTING INFORMATION

Additional figures with energy dispersion X-ray spectroscopy (EDX) and X-ray excited photoelectron spectroscopy (XPS) details are available.

ACKNOWLEDGEMENTS

We would like to acknowledge the Conselho Nacional de Desenvolvimento Científico e Tecnológico (CNPq) (158067/2019- 3) as well Fundação de Amparo à Pesquisa do Estado de São Paulo (2022/02994-2). We would also like to thank the National Nanotechnology Laboratory (LNNano) for allowing us to perform the XPS measurements (XPS-24723).

DECLARATIONS

On behalf of all authors, the corresponding author states that there is no conflict of interest.

DATA AVAILABILITY

The data that supports the findings of this study are available from the corresponding authors upon reasonable request.

REFERENCES

[1] M. Abbasi, U. Rafique, G. Murtaza, M.A. Ashraf, Synthesis, characterisation and photocatalytic performance of ZnS coupled Ag_2S nanoparticles: A remediation model for environmental pollutants, Arabian Journal of Chemistry 11 (2018) 827–837. https://doi.org/10.1016/j.arabjc.2017.12.017.

[2] N. Ameur, F.T. Brahimi, N. Bensaada, H. Gouhas, G. Ferouani, Enhanced Photocatalytic Degradation of Organic Pollutants and Anticorrosion of Mild Steel by Vanadium Modified Titanate Nanotubes (X%V-TiNTs), ChemistrySelect 5 (2020) 13550–13558. https://doi.org/10.1002/slct.202003713.

[3] P. Praipipat, P. Ngamsurach, P. Srirat, P. Chaiphumee, Engineered biosorbents of pomelo (Citrus maxima (Burm.f.) Merr) peels modified with zinc oxide and titanium dioxide for methylene blue dye sorption, Sci Rep 14 (2024). https://doi.org/10.1038/s41598-024-56499-z.

[4] J. Singh, Y.Y. Chang, J.R. Koduru, J.K. Yang, Potential degradation of methylene blue (MB) by nano-metallic particles: A kinetic study and possible mechanism of MB degradation, Environmental Engineering Research 23 (2018) 1–9. https://doi.org/10.4491/eer.2016.158.

[5] N. Wang, J. Chen, J. Wang, J. Feng, W. Yan, Removal of methylene blue by Polyaniline/TiO_2 hydrate: Adsorption kinetic, isotherm and mechanism studies, Powder Technol 347 (2019) 93–102. https://doi.org/10.1016/j.powtec.2019.02.049.

[6] P.K. Jaseela, J. Garvasis, A. Joseph, Selective adsorption of methylene blue (MB) dye from aqueous mixture of MB and methyl orange (MO) using mesoporous titania (TiO_2) – poly vinyl alcohol (PVA) nanocomposite, J Mol Liq 286 (2019) 110908. https://doi.org/10.1016/j.molliq.2019.110908.

[7] X. Jaramillo-Fierro, G. Cuenca, Enhancing Methylene Blue Removal through Adsorption and Photocatalysis—A Study on the GO/$ZnTiO_3$/TiO_2 Composite, Int J Mol Sci 25 (2024). https://doi.org/10.3390/ijms25084367.

[8] H.E. Marr, J.M. Stewart, M.F. Chiu, The crystal structure of methylene blue pentahydrate, Acta Crystallogr B 29 (1973) 847–853. https://doi.org/10.1107/S0567740873003432.

[9] Y. Deng, R. Zhao, Advanced Oxidation Processes (AOPs) in Wastewater Treatment, Curr Pollut Rep 1 (2015) 167–176. https://doi.org/10.1007/s40726-015-0015-z.

[10] T. Yu, H. Chen, T. Hu, J. Feng, W. Xing, L. Tang, W. Tang, Recent advances in the applications of encapsulated transition-metal nanoparticles in advanced oxidation processes for degradation of organic pollutants: A critical review, Appl Catal B 342 (2024) 123401. https://doi.org/10.1016/j.apcatb.2023.123401.

[11] R. Dewil, D. Mantzavinos, I. Poulios, M.A. Rodrigo, New perspectives for Advanced Oxidation Processes, J Environ Manage 195 (2017) 93–99. https://doi.org/10.1016/j.jenvman.2017.04.010.

[12] H.X. Zhu, X.H. Wang, D.F. Zhou, H. Jiang, X.M. Liu, First-principles study on electronic, magnetic properties and optical absorption of vanadium doped rutile TiO_2, Phys Lett A 384 (2020) 126637. https://doi.org/10.1016/j.physleta.2020.126637.

[13] D. Monga, S. Basu, Enhanced photocatalytic degradation of industrial dye by g-C_3N_4/TiO_2 nanocomposite: Role of shape of TiO_2, Advanced Powder Technology 30 (2019) 1089–1098. https://doi.org/10.1016/j.apt.2019.03.004.

[14] D.P. Opra, S. V. Gnedenkov, A.A. Sokolov, A.B. Podgorbunsky, A.Y. Ustinov, V.Y. Mayorov, V.G. Kuryavyi, S.L. Sinebryukhov, Vanadium-doped TiO_2-B/anatase mesoporous nanotubes with improved rate and cycle performance for rechargeable lithium and sodium batteries, J Mater Sci Technol 54 (2020) 181–189. https://doi.org/10.1016/j.jmst.2020.02.068.

[15] D.R. Souza, J.V.S. Neves, Y.K.S. França, W.C. Malheiro, TiO_2 Synthesis by the Pechini's Method and Application for Diclofenac Photodegradation, Photochem Photobiol 97 (2021) 32–39. https://doi.org/10.1111/php.13355.

[16] M.J. Deepa, S.R. Arunima, L. Elias, S.M.A. Shibli, Development of Antibacterial V/TiO_2-Based Galvanic Coatings for Combating Biocorrosion, ACS Appl Bio Mater (2021). https://doi.org/10.1021/acsabm.0c01652.

[17] M.S. Mirghani, Vanadium doped titania nanoparticles for photocatalytic removal of heavy metals from aqueous solutions, J Exp Nanosci 16 (2021) 52–62. https://doi.org/10.1080/17458080.2021.1886277.

[18] Z. Liu, Y. Li, C. Liu, J. Ya, L. E, W. Zhao, D. Zhao, L. An, TiO_2 Photoanode Structure with Gradations in V Concentration for Dye-Sensitized Solar Cells, ACS Appl Mater Interfaces 3 (2011) 1721–1725. https://doi.org/10.1021/am200232g.

[19] J. Liu, Y. Duan, X. Zhou, Y. Lin, Influence of VB group doped TiO_2 on photovoltaic performance of dye-sensitized solar cells, Appl Surf Sci 277 (2013) 231–236. https://doi.org/10.1016/j.apsusc.2013.04.030.

[20] H. Seo, Y. Wang, D. Ichida, G. Uchida, N. Itagaki, K. Koga, M. Shiratani, S.-H. Nam, J.-H. Boo, Improvement on the Electron Transfer of Dye-Sensitized Solar Cell Using Vanadium Doped TiO_2, Jpn J Appl Phys 52 (2013) 11NM02. https://doi.org/10.7567/JJAP.52.11NM02.

[21] B. Roose, S. Pathak, U. Steiner, Doping of TiO_2 for sensitized solar cells, Chem Soc Rev 44 (2015) 8326–8349. https://doi.org/10.1039/C5CS00352K.

[22] O. Sacco, D. Sannino, M. Matarangolo, V. Vaiano, Room Temperature Synthesis of V-Doped TiO_2 and Its Photocatalytic Activity in the Removal of Caffeine under UV Irradiation, Materials 12 (2019) 911. https://doi.org/10.3390/ma12060911.

[23] S.I. Malik, H. Singh, Optical Properties of V-doped TiO_2 Nanocrystals, Arab J Sci Eng 50 (2025) 551–558. https://doi.org/10.1007/s13369-024-09212-1.

[24] A.M. Alotaibi, S. Sathasivam, B.A.D. Williamson, A. Kafizas, C. Sotelo-Vazquez, A. Taylor, D.O. Scanlon, I.P. Parkin, Chemical Vapor Deposition of Photocatalytically Active Pure Brookite TiO_2 Thin Films, Chemistry of Materials 30 (2018) 1353–1361. https://doi.org/10.1021/acs.chemmater.7b04944.

[25] D. Dodoo-Arhin, F.P. Buabeng, J.M. Mwabora, P.N. Amaniampong, H. Agbe, E. Nyankson, D.O. Obada, N.Y. Asiedu, The effect of titanium dioxide synthesis technique and its photocatalytic degradation of organic dye pollutants, Heliyon 4 (2018) e00681. https://doi.org/10.1016/j.heliyon.2018.e00681.

[26] V.M. Ramakrishnan, M. Natarajan, A. Santhanam, V. Asokan, D. Velauthapillai, Size controlled synthesis of TiO_2 nanoparticles by modified solvothermal method towards effective photo catalytic and photovoltaic applications, Mater Res Bull 97 (2018) 351–360. https://doi.org/10.1016/j.materresbull.2017.09.017.

[27] E.S. Rodrigues, M.S. Silva, W.M. Azevedo, S.S. Feitosa, A. Stingl, P.M.A. Farias, ZnO nanoparticles with tunable bandgap obtained by modified Pechini method, Applied Physics A 125 (2019) 504. https://doi.org/10.1007/s00339-019-2805-4.

[28] D.R. Souza, J.V.S. Neves, Y.K.S. França, W.C. Malheiro, TiO_2 Synthesis by the Pechini's Method and Application for Diclofenac Photodegradation, Photochem Photobiol 97 (2021) 32–39. https://doi.org/10.1111/php.13355.

[29] E.S. Rodrigues, M.S. Silva, W.M. Azevedo, S.S. Feitosa, A. Stingl, P.M.A. Farias, ZnO nanoparticles with tunable bandgap obtained by modified Pechini method, Applied Physics A 125 (2019) 504. https://doi.org/10.1007/s00339-019-2805-4.

[30] E.F. de Carli, M. dos Santos, N.A. da Cruz, D.C. Manfroi, J.M. Stropa, L.C.S. de Oliveira, M.A. Zaghete, A.A. Cavalheiro, Effect of Iron and Vanadium on the Phase Transition of Titanium Dioxide Obtained by Polymeric Precursor Method, Materials Science Forum 881 (2016) 18–23. https://doi.org/10.4028/www.scientific.net/MSF.881.18.

[31] D.G. Stroppa, T.R. Giraldi, E.R. Leite, J.A. Varela, E. Longo, Obtenção de filmes finos de TiO_2 nanoestruturado pelo método dos precursores poliméricos, Quim Nova 31 (2008) 1706–1709. https://doi.org/10.1590/S0100-40422008000700020.

[32] W.-F. Chen, S.S. Mofarah, D.A.H. Hanaor, P. Koshy, H.-K. Chen, Y. Jiang, C.C. Sorrell, Enhancement of Ce/Cr Codopant Solubility and Chemical Homogeneity in TiO_2 Nanoparticles through Sol–Gel versus Pechini Syntheses, Inorg Chem 57 (2018) 7279–7289. https://doi.org/10.1021/acs.inorgchem.8b00926.

[33] W. Zhou, Q. Liu, Z. Zhu, J. Zhang, Preparation and properties of vanadium-doped TiO_2 photocatalysts, J Phys D Appl Phys 43 (2010) 035301. https://doi.org/10.1088/0022-3727/43/3/035301.

[34] U. Diebold, T.E. Madey, TiO_2 by XPS, Surface Science Spectra 4 (1996) 227–231. https://doi.org/10.1116/1.1247794.

[35] H. Idriss, On the wrong assignment of the XPS O1s signal at 531–532 eV attributed to oxygen vacancies in photo- and electro-catalysts for water splitting and other materials applications, Surf Sci 712 (2021) 121894. https://doi.org/10.1016/j.susc.2021.121894.

[36] Y. Zhu, D. Liu, M. Meng, H_2 spillover enhanced hydrogenation capability of TiO_2 used for photocatalytic splitting of water: a traditional phenomenon for new applications, Chem. Commun. 50 (2014) 6049–6051. https://doi.org/10.1039/C4CC01667J.

[37] K.K. Rahangdale, S. Ganguly, Effect of oxygen vacancies on the dielectricity of Ga doped equimolar $BiMnO_3$–$BaTiO_3$ characterized by XPS analysis, Physica B Condens Matter 626 (2022) 413570. https://doi.org/10.1016/j.physb.2021.413570.

[38] G. Silversmit, D. Depla, H. Poelman, G.B. Marin, R. De Gryse, Determination of the V2p XPS binding energies for different vanadium oxidation states (V^{5+} to V^{0+}), J Electron Spectros Relat Phenomena 135 (2004) 167–175. https://doi.org/10.1016/j.elspec.2004.03.004.

[39] A. Godoy Junior, A. Pereira, M. Gomes, M. Fraga, R. Pessoa, D. Leite, G. Petraconi, A. Nogueira, H. Wender, W. Miyakawa, M. Massi, A. da Silva Sobrinho, Black TiO_2 Thin Films Production Using Hollow Cathode Hydrogen Plasma Treatment: Synthesis, Material Characteristics and Photocatalytic Activity, Catalysts 10 (2020) 282. https://doi.org/10.3390/catal10030282.

[40] H. Song, C. Li, Z. Lou, Z. Ye, L. Zhu, Effective Formation of Oxygen Vacancies in Black TiO_2 Nanostructures with Efficient Solar-Driven Water Splitting, ACS Sustain Chem Eng 5 (2017) 8982–8987. https://doi.org/10.1021/acssuschemeng.7b01774.

[41] A. Sarkar, G.G. Khan, The formation and detection techniques of oxygen vacancies in titanium oxide-based nanostructures, Nanoscale 11 (2019) 3414–3444. https://doi.org/10.1039/C8NR09666J.

[42] N. Khatun, E.G. Rini, P. Shirage, P. Rajput, S.N. Jha, S. Sen, Effect of lattice distortion on bandgap decrement due to vanadium substitution in TiO_2 nanoparticles, Mater Sci Semicond Process 50 (2016) 7–13. https://doi.org/10.1016/j.mssp.2016.04.002.

[43] T. Wang, T. Xu, Effects of vanadium doping on microstructures and optical properties of TiO_2, Ceram Int 43 (2017) 1558–1564. https://doi.org/10.1016/j.ceramint.2016.10.132.

[44] M. HORN, C.F. SCHWEBDTFEGER, E.P. MEAGHER, Refinement of the structure of anatase at several temperatures, Z Kristallogr Cryst Mater 136 (1972) 273–281. https://doi.org/10.1524/zkri.1972.136.16.273.

[45] T.J.B. Holland, S.A.T. Redfern, Unit cell refinement from powder diffraction data: the use of regression diagnostics, Mineral Mag 61 (1997) 65–77. https://doi.org/10.1180/minmag.1997.061.404.07.

[46] R.D. Shannon, Revised effective ionic radii and systematic studies of interatomic distances in halides and chalcogenides, Acta Crystallographica Section A 32 (1976) 751–767. https://doi.org/10.1107/S0567739476001551.

[47] R. Kaur, P. Singla, K. Singh, Transition metals (Mn, Ni, Co) doping in TiO_2 nanoparticles and their effect on degradation of diethyl phthalate, International Journal of Environmental Science and Technology 15 (2018) 2359–2368. https://doi.org/10.1007/s13762-017-1573-y.

[48] A.O. Bokuniaeva, A.S. Vorokh, Estimation of particle size using the Debye equation and the Scherrer formula for polyphasic TiO_2 powder, J Phys Conf Ser 1410 (2019) 012057. https://doi.org/10.1088/1742-6596/1410/1/012057.

[49] J. Choi, H. Park, M.R. Hoffmann, Combinatorial doping of TiO_2 with platinum (Pt), chromium (Cr), vanadium (V), and nickel (Ni) to achieve enhanced photocatalytic activity with visible light irradiation, J Mater Res 25 (2010) 149–158. https://doi.org/10.1557/JMR.2010.0024.

[50] E. Kroumova, M.I. Aroyo, J.M. Perez-Mato, A. Kirov, C. Capillas, S. Ivantchev, H. Wondratschek, Bilbao Crystallographic Server: Useful Databases and Tools for Phase-Transition Studies, Phase Transitions 76 (2003) 155–170. https://doi.org/10.1080/0141159031000076110.

[51] A. Shirpay, M. Tavakoli, The behavior of the active modes of the anatase phase of TiO_2 at high temperatures by Raman scattering spectroscopy, Indian Journal of Physics 96 (2022) 1673–1681. https://doi.org/10.1007/s12648-021-02123-z.

[52] T. Ohsaka, F. Izumi, Y. Fujiki, Raman spectrum of anatase, TiO_2, Journal of Raman Spectroscopy 7 (1978) 321–324. https://doi.org/10.1002/jrs.1250070606.

[53] A.R. Zanatta, Temperature-dependent optical bandgap of TiO_2 under the Anatase and Rutile phases, Results Phys 60 (2024) 107653. https://doi.org/10.1016/j.rinp.2024.107653.

[54] F. Tian, Y. Zhang, J. Zhang, C. Pan, Raman Spectroscopy: A New Approach to Measure the Percentage of Anatase TiO_2 Exposed (001) Facets, The Journal of Physical Chemistry C 116 (2012) 7515–7519. https://doi.org/10.1021/jp301256h.

[55] M. Scepanovic, M. Grujic-Brojcin, Z.D. Dohcevic-Mitrovic, Z.V. Popovic, Characterization of anatase TiO_2 nanopowder by variable-temperature Raman spectroscopy, Science of Sintering 41 (2009) 67–73. https://doi.org/10.2298/SOS0901067S.

[56] J.H. De Boer, Adsorption Phenomena, in: 1956: pp. 17–161. https://doi.org/10.1016/S0360-0564(08)60538-6.

[57] A. Dąbrowski, Adsorption — from theory to practice, Adv Colloid Interface Sci 93 (2001) 135–224. https://doi.org/10.1016/S0001-8686(00)00082-8.

[58] P. Pourhakkak, A. Taghizadeh, M. Taghizadeh, M. Ghaedi, S. Haghdoust, Fundamentals of adsorption technology, in: Interface Science and Technology, Elsevier B.V., 2021: pp. 1–70. https://doi.org/10.1016/B978-0-12-818805-7.00001-1.

[59] X. Liang, S. Zhu, Y. Zhong, J. Zhu, P. Yuan, H. He, J. Zhang, The remarkable effect of vanadium doping on the adsorption and catalytic activity of magnetite in the decolorization of methylene blue, Appl Catal B 97 (2010) 151–159. https://doi.org/10.1016/j.apcatb.2010.03.035.

[60] B. Wang, F.C. de Godoi, Z. Sun, Q. Zeng, S. Zheng, R.L. Frost, Synthesis, characterization and activity of an immobilized photocatalyst: Natural porous diatomite supported titania nanoparticles, J Colloid Interface Sci 438 (2015) 204–211. https://doi.org/10.1016/j.jcis.2014.09.064.

[61] J. Wang, X. Guo, Adsorption kinetic models: Physical meanings, applications, and solving methods, J Hazard Mater 390 (2020) 122156. https://doi.org/10.1016/j.jhazmat.2020.122156.

[62] A.N. Ebelegi, N. Ayawei, D. Wankasi, Interpretation of Adsorption Thermodynamics and Kinetics, Open J Phys Chem 10 (2020) 166–182. https://doi.org/10.4236/ojpc.2020.103010.

[63] T.-B. Nguyen, M.-J. Hwang, K.-S. Ryu, High adsorption capacity of V-doped TiO_2 for decolorization of methylene blue, Appl Surf Sci 258 (2012) 7299–7305. https://doi.org/10.1016/j.apsusc.2012.03.148.

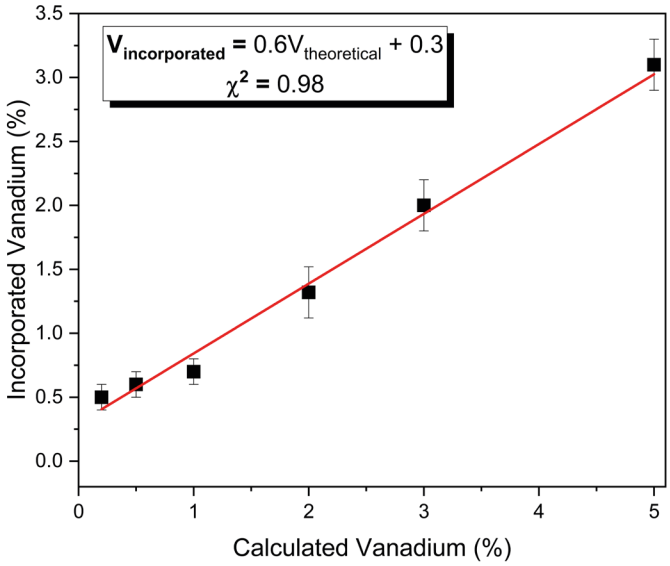

Figure S1. Incorporated vanadium percentage as a function of the calculated vanadium, obtained from EDX measurements. The red line represents the linear fit to the experimental data.

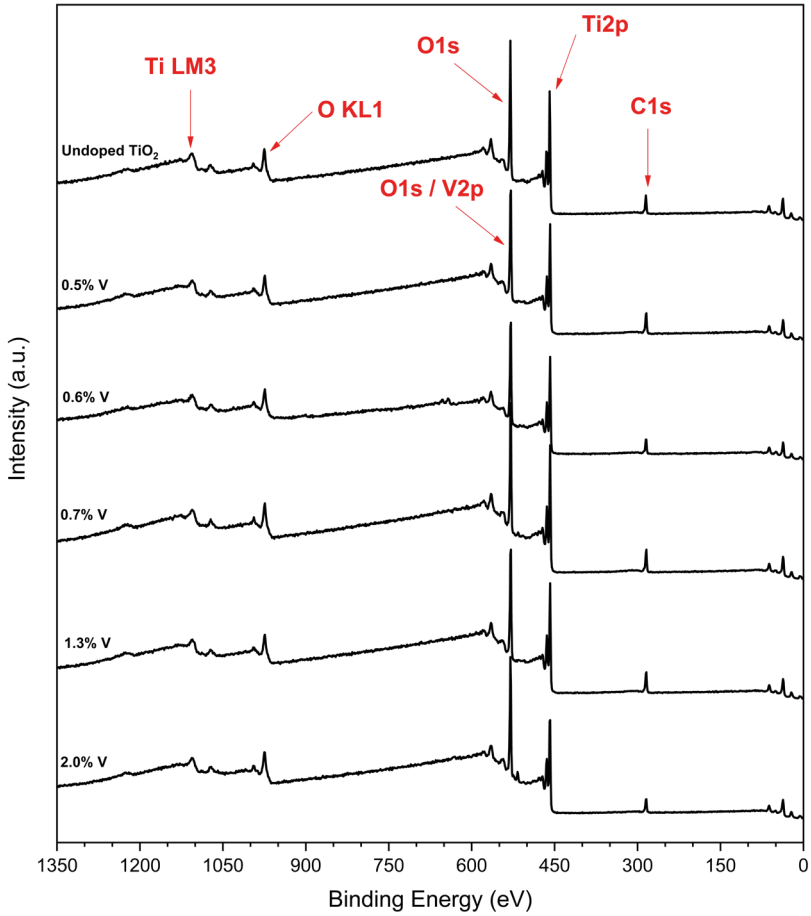

Figure S2. XPS survey spectra for pure and V-doped TiO_2 samples.

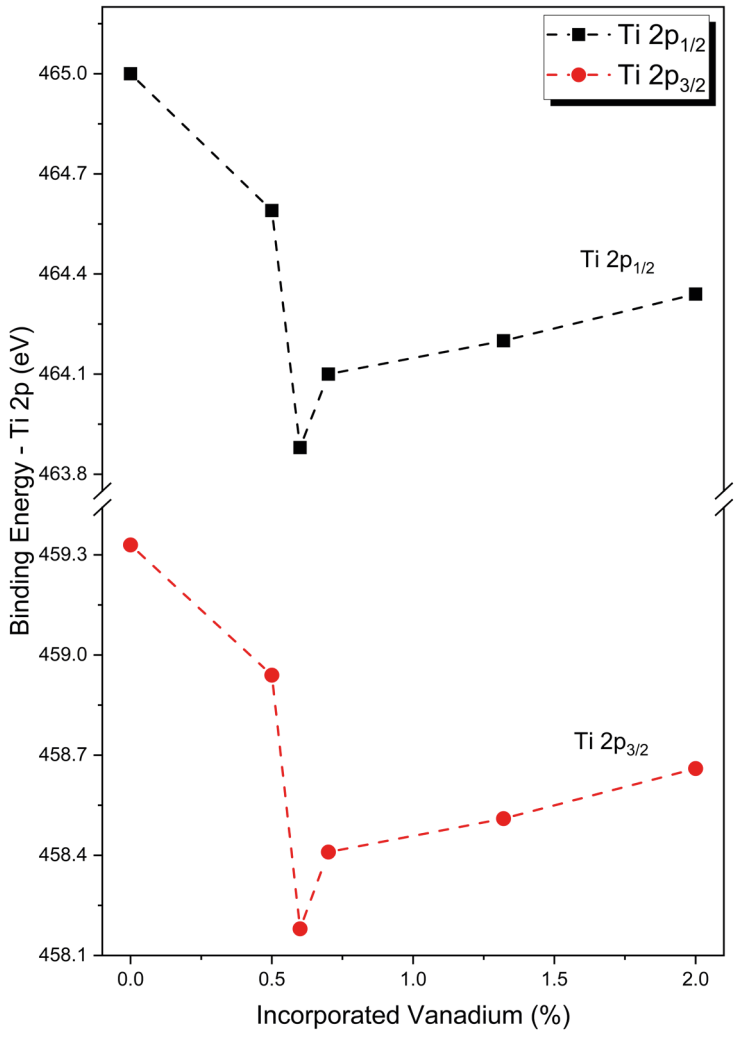

Figure S3. Ti 2p binding energy as a function of vanadium doping percentage. (Dashed lines were employed to facilitate interpretation of the data.)

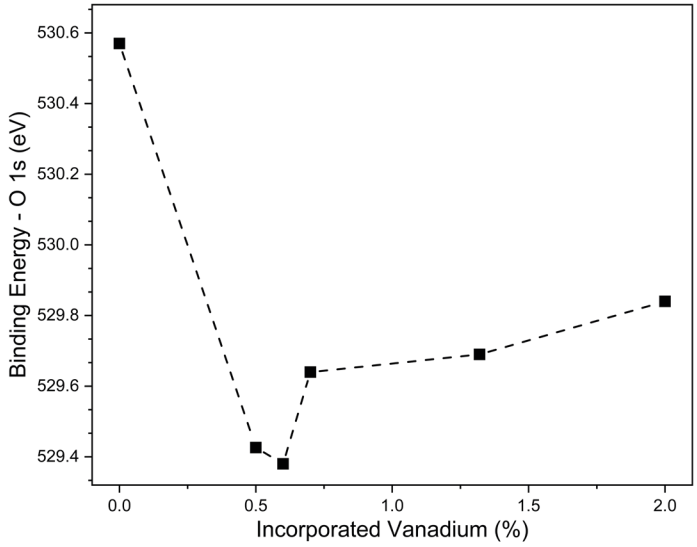

Figure S4. O 1s binding energy as a function of vanadium doping percentage. (Dashed lines were employed to facilitate interpretation of the data.)